Constraining the Black Hole Mass Spectrum with Gravitational Wave Observations I: The Error Kernel

Joseph E. Plowman[1], Daniel C. Jacobs[1], Ronald W. Hellings[1],
Shane L. Larson[2], Sachiko Tsuruta[1]

ABSTRACT

Many scenarios have been proposed for the origin of the supermassive black holes (SMBHs) that are found in the centres of most galaxies. Many of these formation scenarios predict a high-redshift population of intermediate-mass black holes (IMBHs), with masses $M_\bullet$ in the range $10^2 M_\odot \lesssim M_\bullet \lesssim 10^5 M_\odot$. A powerful way to observe these IMBHs is via gravitational waves the black holes emit as they merge. The statistics of the observed black hole population should, in principle, allow us to discriminate between competing astrophysical scenarios for the origin and formation of SMBHs. However, gravitational wave detectors such as LISA will not be able to detect all such mergers nor assign precise black hole parameters to the merger, due to weak gravitational wave signal strengths. In order to use LISA observations to infer the statistics of the underlying population, these errors must be taken into account. We describe here a method for folding the LISA gravitational wave parameter error estimates into an 'error kernel' designed for use at the population model level. The effects of this error function are demonstrated by applying it to several recent models of black hole mergers, and some tentative conclusions are made about LISA's ability to test scenarios of the origin and formation of supermassive black holes.

Subject headings: Black Hole Physics - Early Universe - Gravitational Waves - Methods: Statistical

1. Introduction

There is now substantial evidence (e.g., Kormendy & Richstone 1995; Richstone et al. 1998; Bender 2005; Rees 2002, 2003) for the existence of supermassive black holes (SMBHs) in the nuclei of most galaxies, the black hole in our own galaxy being the best studied and most clearly justified of these objects. However, the origin of these black holes remains an unsettled question. In one scenario, the more massive black holes formed from the merger and coalescence of smaller 'seed' black holes that were created in the very early Universe (e.g., Madau & Rees 2001). Several models

---

[1]Department of Physics, Montana State University, Bozeman, MT 59717

[2]Department of Physics, Utah State University, Logan, UT 84322

utilizing this process have been proposed and numerically simulated (e.g., Haehnelt & Kauffmann 2000; Volonteri et al. 2003). In (e.g., Volonteri et al. 2003; Tanaka & Haiman 2009), typical seed black holes are the remnants of Population III stars with masses $m_\bullet \sim 100 - 300 M_\odot$ formed at high redshift (e.g., $z \sim 20$ – 50). Thus, these models predict an evolving population of intermediate mass black holes (IMBHs), with masses between ~ 100 to $10^5 M_\odot$.[1] In another version (Begelman et al. 2006), the seed black holes are formed due to direct collapse of the cores of pregalactic halos through a 'quasi-star' stage, resulting in a more massive seed population ($\sim 10^4 - 10^6 M_\odot$). This scenario predicts far fewer IMBHs in the early universe.

Black holes in the IMBH mass range are extremely difficult to detect with the usual electromagnetic observation techniques, making it very difficult to verify a particular formation and evolution scenario and, especially, to discriminate between various models. However, the mergers themselves produce gravitational waves in the Low Frequency (LF) band, from 10^{-6} Hz to 10^{-1} Hz, probed by the proposed LISA mission (Jennrich 2004). Observations of the amplitude, frequency chirp, and harmonic structure of the gravitational wave waveform enable both the luminosity distance and the individual masses of the black holes in the binary system to be determined. LF gravitational wave observations thus provide a probe of the cosmological spectrum of black holes, and allow tests of the population models to be made. In this paper, we investigate how gravitational wave observations of coalescing massive black hole binaries may be used to discriminate between models of massive black hole populations and determine the merger history that has led to the observed population of SMBHs.

We thus take a slightly different direction, compared to other recent works investigating LISA detections of black hole coalescences. Most of these take the somewhat speculative black hole population models and calculate the number of coalescences that each model predicts would be observed by LISA. The scientific goal of these papers has clearly been the observation of the coalescence itself. In this paper, we turn the problem around and ask, 'What might LISA observations of binary MBH coalescences tell us about the otherwise uncertain population models?'

The organization of the paper is as follows. In Section 2, we discuss some of the population models and the motivation behind them. Section 3 describes the parameters relevant to detection of a black hole binary and draws a distinction between 'population' parameters, which are relevant to the population models, and astrophysically uninteresting 'sample' parameters, which vary randomly for each sample drawn from a population. We also review the response of the LISA gravitational wave detector to massive black hole binary coalescences, with emphasis on the ability of the detector to determine the parameters of the binary from the gravitational wave waveform. The bulk of our work is presented in Section 4, which describes a Monte Carlo calculation of an 'error kernel', which is marginalised over the sample parameters. This error kernel, $K(\hat{\lambda}_i, \lambda_i)$, is the average conditional probability that a source will be detected with population parameters $\hat{\lambda}_i$ in the LISA data, given

---

[1]Since our studies include both IMBHs, with mass $\sim 100 M_\odot$ to $10^5 M_\odot$, and SMBHs, with mass $\sim 10^5 M_\odot$ to $10^9 M_\odot$, we adopt the terminology 'massive black hole' (MBH) to cover the entire range from $\sim 100 M_\odot$ to $10^9 M_\odot$.

the existence of an astrophysical source with population parameters λ_i. The marginalisation over sample parameters sets this apart from previous work, and the resulting error kernels can be applied directly to model coalescence rates, producing a new set of coalescence rates as functions of the best-fitting, 'detected', parameter values. Finally, in Section 5, we take several population models from the literature and discuss how the error kernel may be used to produce a measure of how well the models may be discriminated from one another. Although the models we use are incomplete, being based only on summaries available in the literature, we nevertheless draw a few tentative conclusions about LISA's ultimate ability to distinguish between black hole population models in Section 6.

2. Astrophysical Populations of Black Hole Binary Systems

Observations of the high redshift quasar population (Fan et al. 2001; Stern et al. 2000; Zheng et al. 2000; Becker et al. 2001) suggest that a population of SMBHs has existed since early epochs ($z \sim 6$). The local census of SMBHs has been increasing in recent years (Tremaine et al. 2002), driven by a growing body of observational evidence linking the mass of SMBHs with observational properties of their host galaxies. Early studies revealed a rough correlation between SMBH mass and the bulge luminosity of the host galaxy (Kormendy & Richstone 1995; Magorrian et al. 1998). A much stronger correlation was later discovered between the SMBH mass and the stellar velocity dispersion in the galactic core, the so-called 'M-σ' relation (Gebhardt et al. 2000; Ferrarese & Merritt 2000; Tremaine et al. 2002). The current best fit to the M-σ relation (Merritt & Ferrarese 2001; Tremaine et al. 2002) gives the mass of the central black hole $M_\bullet$ as

$$\log\left(\frac{M_\bullet}{M_\odot}\right) = 8.13 + 4.02 \log\left(\frac{\sigma}{200\text{km/s}}\right) \ . \tag{1}$$

The observational data supporting the $M - \sigma$ relation currently spans a mass range from $\sim 10^5 M_\odot$ to $\sim 10^9 M_\odot$.

Given this observational evidence for the existence of a SMBH population, the question arises: how did these objects come to be? Several scenarios are proposed (see Djorgovski et al. 2008):

1. direct gravitational core collapse of pregalactic dark halos,

2. growth from seed black holes through merging and coalescences over time,

3. gravitational runaway collapse of dense star clusters,

4. primordial BH remnants from the big bang.

In case 1 SMBHs can form very early in the Universe through direct collapse of dark matter halo with mass of $\sim 10^6 M_\odot$ or larger (Bromm & Loeb 2002). In case 2, on the other hand, (Madau &

Rees 2001; Haehnelt & Kauffmann 2000; Volonteri et al. 2003; Tanaka & Haiman 2009; Begelman et al. 2006), seed black holes produced in the early universe are significantly smaller and grow by accretion, coalescences and merging, leading to the population of SMBHs seen in the Universe today. In most cases (e.g., Volonteri et al. 2003) the seed black holes have mass less than $\sim 300 M_\odot$, and are the remnants of ordinary Population III stars. Detailed stellar evolution calculations have recently found, however, that these seed black holes can be remnants of very massive Population III stars, referred to as CVMSs (Ohkubo et al. 2006, 2008; Tsuruta et al. 2007; Ohkubo et al. 2009; Umeda et al. 2009). These metal-free CVMSs evolve quickly and then collapse in the early universe, yielding an IMBH population with masses in the range of $\sim 500 M_\odot - 10,000 M_\odot$. In another version (Begelman et al. 2006), even more massive black holes can form from direct core collapse of mini halos through a quasi-star phase, instead of through ordinary stellar evolution, leading to a population with masses in the range $\sim 10^4 \mathrm{M}_\odot$ to $\sim 10^6 \mathrm{M}_\odot$.

The scenario involving direct collapse is not difficult to distinguish from that involving Population III stars, because the former predicts only a small number of the more massive IMBHs while the latter predicts considerably more IMBHs with a wider range of masses and redshifts. In case 3 (e.g., Ebisuzaki et al. 2001; Portegies Zwart et al. 2004a,b), IMBHs can be formed at any time in dense star clusters and grow by merging in the given environment. Such a process can produce a low level population of mergers at all redshifts. Case 4 is theoretically possible, but currently it will be hard to test by observations.

In this paper, we concentrate on versions of case 2, although the techniques used are general and should also apply to discrimination between other MBH population scenarios. Specifically, we use the results published in Sesana et al. (2007), which give coalescence rates for models discussed in Volonteri et al. (2003), Koushiappas et al. (2004), and Begelman et al. (2006). In these models, the evolution of the seed population through time is carried out numerically (Somerville & Kolatt 1999; Volonteri et al. 2003). In Volonteri et al. (2003), for instance, the evolution of a SMBH's host galaxy halo is first computed, starting at the present day and working backwards in time to $z \sim 20$. Then, the progenitor haloes are seeded with BHs of $150 M_\odot$, and the BH merger history is traced forward in time through the halo merger history. Major differences between different versions of this scenario come from the varying astrophysical assumptions employed - e.g., the initial conditions, environment, age (the redshifts when the seeds were produced), seed mass, dynamics, hierarchial growth, etc., built into the process.

3. Gravitational wave binaries

3.1. Binary Parameters

Each black hole binary may be characterized by a number of parameters, which are usually divided into two categories. The first category is the *intrinsic* parameters which have to do with the local properties of the binary in its rest frame. They are m_1, the mass of the primary, m_2,

the mass of the secondary, and either the initial orbital separation, a, frequency, f (related to a by Kepler's third law) or time to coalescence, t_c, (related to a by the quadrupole formula)[2]. A set of mass parameters equivalent to m_1 and m_2 but more directly related to the gravitational wave waveform, is the chirp mass $\mathcal{M}_c = (m_1 m_2)^{3/5}(m_1 + m_2)^{-1/5}$ and the symmetric reduced mass ratio $\eta = (m_1 m_2)/(m_1 + m_2)^2$. Note that, in the gravitational wave signal, the masses are scaled by the redshift, so that the natural mass variables for gravitational wave data analysis are redshifted. For instance, the redshifted chirp mass is $\mathcal{M}_c \times (1 + z)$, although the reduced mass ratio remains unchanged since it is dimensionless. The remaining parameters fall into the second category, and are called *extrinsic* parameters. These have to do with the binary's location and orientation with respect to the LISA constellation. They are the luminosity distance D_L (or equivalently, the redshift z), the principle gravitational wave polarization angle ψ, the binary inclination ι, the sky location angles θ and ϕ, and the initial phase of the binary orbit Φ_0.

Redshift and luminosity distance are used interchangeably as source parameters, with the relationship between them determined from the standard WMAP cosmology ($\Omega_M = 0.27$, $\Omega_{\mathrm{vac}} = 0.73$, $\Omega_{\mathrm{rad}} = 0.0$, and a Hubble constant of 71 km/s/Mpc).

Since the predictions of the population studies are given as functions of masses and redshift, the binary parameters are best divided into two sets in a *different* way, for purposes of this paper. The first set, consisting of $\mathcal{M}_c$, η, and z, are what we will call *population* parameters, since these are the parameters that characterise the population model predictions. The remaining parameters, ψ, ι, θ, ϕ, t_c, and Φ_0, represent particular samples drawn from the population model and will be referred to as *sample* parameters. Sample parameters have distributions that are essentially stochastic and contain no useful information about the astrophysical processes which give rise to the black hole population.

Despite the fact that the sample parameters are not part of the intrinsic astrophysical model, they can have a dramatic effect on LISA's source characterisation capabilities because all parameters must be fit to the data in the process of extracting the population parameters of interest. A key component of this analysis is therefore to calculate average LISA error distributions for the population parameters by averaging over a Monte Carlo ensemble of many sources, each having randomly-chosen values for the sample parameters. Such error distributions are referred to as 'error kernels'.

3.2. Gravitational Waves from Binary Systems

Calculation of the detectability of binary systems via gravitational wave emission is a standard problem in the gravitational wave community; see, for instance, Flanagan & Hughes (1998a,b), and

---

[2]In general, the list of intrinsic parameters also includes the black hole spins and orbital eccentricity. Here, however, attention is restricted to the simplified case of non-spinning black holes in circular orbits.

Cutler & Flanagan (1994). We review the problem here for convenience and locality of reference.

Spin interactions and higher order post-Newtonian corrections are neglected in this paper, although they can have an appreciable effect on parameter error estimation. For instance, Hellings & Moore (2003) have shown that the inclusion of higher harmonics of the waveform would improve the determination of the mass parameter η, while Lang & Hughes (2006) have shown that spinning black holes produce a modulation in the signal that leads to a tighter bound on the sky position of the binary.

The dimensionless gravitational wave strain produced by a circularised binary can be written as the superposition of two independent polarization states h_+ and $h_\times$. The polarization amplitudes can be expanded in terms of harmonics as

$$h_{+,\times}(\tau) = \sum_n h_{+,\times}^{(n)} \exp[in\Phi(\tau)], \tag{2}$$

where $\tau = t - \hat{k} \cdot \vec{x}$ locates the surface of constant phase for a gravitational wave propagating in a direction $\hat{k}$, and $\Phi(\tau)$ is the phase of the binary orbit, as observed at the LISA detector. When the binary is far from coalescence, the dominant emission is the $n = 2$ quadrupole, which is

$$
\begin{aligned}
h_+(\tau) &= \frac{2\mathcal{M}_c \left[\pi f\right]^{2/3}}{D_L}(1 + \cos^2 \iota) \cos\left[2\Phi(\tau)\right] \\
h_\times(\tau) &= -\frac{4\mathcal{M}_c \left[\pi f\right]^{2/3}}{D_L} \cos \iota \sin\left[2\Phi(\tau)\right]
\end{aligned}
\tag{3}
$$

where f is the fundamental quadrupole frequency, $f = 2(d\Phi/dt)/(2\pi)$. We note that h_+ and $h_\times$ are still functions of the observed time τ.

The response of the LISA detector to the two polarizations of a gravitational wave from a binary is given by

$$y(\tau) = F_+(\theta, \phi, \iota, \psi, \tau)h_+(\tau) + F_\times(\theta, \phi, \iota, \psi, \tau)h_\times(\tau) \tag{4}$$

where F_+ and $F_\times$ are the LISA form factors that depend on the position and orientation of the source relative to the time-dependent LISA configuration.

3.3. Detecting Black Hole Binaries

One measure of the ability of the LISA detector to observe a binary signal is the signal-to-noise ratio, defined as

$$(\text{SNR})^2 = 4 \int_0^\infty \frac{|\widetilde{h}(f)|^2}{S_{\text{LISA}}(f)} \, df \, , \tag{5}$$

where $|\widetilde{h}(f)|^2 = |\widetilde{h}_+(f)|^2 + |\widetilde{h}_\times(f)|^2$, with $\widetilde{h}_+(f)$ and $\widetilde{h}_\times(f)$ being the Fourier transforms of the polarization amplitudes in equation 3, and where $S_{\text{LISA}}(f)$ is the apparent noise level of LISA's Standard Curve Generator (Larson (2000), hereafter SCG), an estimate that averages the LISA response over the entire sky and over all polarization states and divides the LISA instrument noise, $S_n(f)$, by this averaged response.

Previous treatment of LISA observations of binary black hole populations (Sesana et al. 2007) have employed this measure of detectability, while others (Sesana et al. 2004) have used a characteristic strain h_c, following the prescription of Thorne (1987). In this measure, the raw strain h of a source is multiplied by the average number of cycles of radiation emitted over a frequency interval $\Delta f = 1/T_{obs}$ centred at frequency f. The amplitude of the characteristic strain is then compared directly against the 1-year averaged strain sensitivity curve from the SCG to produce an SNR. In either case, a source is considered detectable if the resulting SNR exceeds some standard threshold value (typically between 5 and 10).

While interesting for planning LISA data analysis pipelines, these SNR estimates fail to address the fact that a detection is of little use for comparison with astrophysical theory if the parameters of the binary are poorly determined. In particular, unless the masses and redshifts of the detected black holes are measured, the observations cannot be compared with the black-hole evolution models. A more complete analysis that incorporates the effects of uncertainty in the binary parameters is required.

Parameter error estimation for black hole binaries detected via gravitational wave emission has been discussed by many researchers (Cutler & Flanagan 1994; Vallisneri 2008; Moore & Hellings 2002; Crowder 2006). This section reviews the covariance analysis for a *linear least squares* process, based on the Fisher information matrix, the method which forms the core of the error analysis in this paper.

Let us suppose that the LISA combined data stream consists of discrete samples of a signal given by (Eq. 4), with added noise:

$$s_\alpha = y_\alpha(\lambda_i) + n_\alpha \tag{6}$$

Here, λ_i are the parameters of the source and n_α is the noise, assumed to be stationary and Gaussian. The probability distribution of the αth data point is therefore

$$p(s_\alpha|\lambda_i) = \frac{1}{\sqrt{2\pi\sigma_\alpha^2}} \times e^{-\frac{1}{2}[s_\alpha - y_\alpha(\lambda_i)]^2/\sigma_\alpha^2}, \tag{7}$$

where σ_α (with Greek subscript) is the standard deviation of the noise in the αth data point.

The likelihood function for a particular data set, with parameters λ_i, is the product of the

probabilities (Eq. 7) for each data point. It is

$$L(s_\alpha|\lambda_j) \propto \exp\left[-\sum_i \frac{1}{2}\frac{[s_\alpha - y_\alpha(\lambda_j)]^2}{\sigma_\alpha^2} \right] \qquad (8)$$

The set of parameters, $\hat{\lambda}_i$, that maximizes the likelihood function is an unbiased estimate of the the set of actual model parameters, λ_i. To calculate the $\hat{\lambda}_i$, we assume that the differences between the estimated values and the true values, $\Delta\hat{\lambda}_i \equiv \hat{\lambda}_i - \lambda_i$ are small enough that $y_\alpha(\hat{\lambda}_i)$ can be approximated by its first-order Taylor series expansion about λ_i:

$$y_\alpha(\hat{\lambda}_k) \approx y_\alpha(\lambda_k) + \nabla_i y_\alpha \Delta\hat{\lambda}_i. \qquad (9)$$

where ∇_i represents the partial derivative with respect to λ_i. This first-order expansion is valid when the SNR is high enough, and the degree of correlation between the parameters is low enough that the resulting $\Delta\lambda_i$ are small. Using Eq. 8 we find[3] that the likelihood is maximized by

$$\Delta\lambda_i = (\mathbf{F}^{-1})_{ij}\sum_\alpha \frac{1}{2}\frac{(s_\alpha - y_\alpha)\nabla_j y_\alpha}{\sigma_\alpha^2}, \qquad (10)$$

where the matrix $\mathbf{F}$ is the *Fisher information matrix*, with components

$$F_{ij} = \sum_\alpha \frac{1}{2\sigma_\alpha^2}\nabla_i y_\alpha \nabla_j y_\alpha. \qquad (11)$$

The expected parameter covariance matrix is

$$\langle \Delta\lambda_i \Delta\lambda_j \rangle = F_{ij}^{-1} \qquad (12)$$

The standard deviations in each detected parameter, σ_i (with Latin subscript), are given by the diagonal elements of the covariance matrix:

$$\sigma_i^2 = F_{ii}^{-1} \qquad \text{(no sum over } i\text{)} \qquad (13)$$

It is important to remember that the Fisher error estimate is accurate only when the parameter uncertainties are small compared to the characteristic scales of the system being fit (Vallisneri & Mock LISA Data Challenge Taskforce 2006), a condition that is not well satisfied for all of the binaries being modelled here. In these cases, however, the method tends to overestimate the degree of uncertainty in systems with a sharply-defined minimum, and the resulting error estimates tend to be conservative.

Rather than write our own Fisher error estimation codes, we have made use of the publicly available LISA Calculator (Crowder & Cornish 2006; Crowder 2006). The LISA Calculator uses the same instrument noise model $S_n(f)$ that is used as input to the SCG, and an analytic signal

---

[3]It is also necessary to keep only terms that are first order in the inverse of the SNR; see Vallisneri (2008)

model given by Eqs. 3 and 4. It takes as input a set of source parameter values, λ_j, and outputs a set of standard deviations (equation 13), σ_i, for the detected parameter values, $\hat{\lambda}_i$. Each detected parameter, $\hat{\lambda}_i$, is assumed to have a Gaussian probability density with mean λ_i and standard deviation σ_i,

$$p_D(\hat{\lambda}_i|\lambda_i) = \frac{1}{\sqrt{2\pi\sigma_i^2}} \exp\left[-\frac{\left[\hat{\lambda}_i - \lambda_i\right]^2}{2\sigma_i^2}\right]. \tag{14}$$

4. The Error Kernel

The output of the astrophysical models of interest can be described in terms of a coalescence rate, $\Gamma(M, \eta, z)$, per unit redshift and time. However, the coalescence rate observed in the LISA detector, $\Gamma'(\hat{M}, \hat{\eta}, \hat{z})$, will differ from $\Gamma(M, \eta, z)$ because some sources will be too weak to be detected and because errors in the LISA parameter determination will assign incorrect parameters to the source, due to the effect of the noise on the estimation process. The effect of these errors is summed up in the LISA error kernel, K:

$$\Gamma'(\hat{M}, \hat{\eta}, \hat{z}) = \int_{\text{pop}} \Gamma(M, \eta, z) \times \epsilon(M, \eta, z)$$
$$\times K(\hat{M}, \hat{\eta}, \hat{z}|M, \eta, z) \, dz \, d\eta \, dM, \tag{15}$$

where $\epsilon(M, \eta, z)$ is the average detectability of a source with parameters $\{M, \eta, z\}$ in the LISA detector.

4.1. Calculating the Error Kernel

As discussed in Section 3.1, coalescence rates given by the various models are functions of the *population* parameters only. They do not depend on the *sample* parameters, which arise from the random relationship between the observer and a particular binary in the population. We therefore produce a Monte Carlo average or 'marginalisation' over the sample parameters, compiling the Fisher matrix error estimates into an 'Error Kernel' which is a function of sample parameters only.

Since we have no *a priori* reason to expect inhomogeneous or anisotropic distribution, the values of the extrinsic sample parameters of a black hole binary are assumed to be uniformly distributed – angular location and orientation variables are uniformly distributed on the sky, and Φ_0 is uniformly distributed over the interval $[0, 2\pi]$ (see Table 1).

The appropriate distribution to use for t_c is somewhat more complicated, owing to two primary considerations. First, astrophysical models of the MBH population are usually expressed in terms of the number of coalescences per unit time and redshift. Second, the LISA detectability of a

binary (generally related to SNR) is a monotonically decreasing function of the binary's t_c (all else being equal) for t_c longer than the LISA observation time T_{obs}. Because of their relatively stronger signals, binaries coalescing inside or soon after the LISA observation lifetime window are far more likely to be detected than those with long times to coalescence, so those with long times to coalescence represent a negligible fraction of the set of detected binaries. In calculating the error kernel, we found that the number of additional detected sources coalescing in the year following the end of LISA observation was a negligible fraction of the total, and decided to simply use a 1 year observation time and range of tc for most of our results, multiplying by 3 to get results for a 3 year observation. We found that the results were not significantly different from, for instance, using a full 3 year observation time and 4 year range of tc.

While the binary masses are also population parameters, the models we have found in the literature generally divide their mass spectra into very wide logarithmic bins or give no mass spectra at all. Since the mass also has a significant effect on the detectability and parameter estimation error of a source, however, we cannot simply generate masses completely at random or treat them in some other trivial fashion. We therefore partially marginalize over the mass and attempt to make a reasonable choice for the mass distribution within the mass bins published in the literature. This choice of mass distribution is somewhat problematic, since additional information on the mass distribution is available for some of the models studied (Volonteri et al. (2003), for instance), but not for others. Even if useful information on the mass distribution were available for all of the models studied, we prefer not to tailor intra-bin mass distributions to each particular model, because we want the error kernels to be model-independent. We have decided, for purposes of this paper, to use a simple uniform logarithmic distribution within each mass bin. While this distribution can produce significant differences in detection rates for the coarsely-binned models studied here, our opinion is that it remains a reasonable choice for a model independent intra-bin mass distribution, and such problems are best solved by increasing the mass resolution of the reported model results. For similar reasons, we also completely marginalise over mass ratio. We use the three mass ranges found in Sesana et al. (2007) for our mass bins. The redshift is not marginalised, and separate Monte Carlo runs are made at uniformly spaced values of z ranging from $0 \ldots 20$ (see Table 1) and the statistics are collected as a function of redshift. The 'population' parameter space is thus considered as a collection of two-dimensional volume elements chosen from the three mass bins and up to 80 bins in redshift.

Within each volume element, values for the marginalised parameters are chosen randomly and a covariance error analysis is performed, with the probability distribution function (PDF) for each sample being calculated using Eq. 14. A typical single PDF for one sample is shown in Figure 1a. PDFs from the random sampling of the source parameters are stored and averaged, producing a PDF for the population parameters corresponding to the source volume element chosen. An example of a marginalised PDF is shown in Figure 1b. This conditional probability – the probability of LISA assigning a particular redshift to a source, given that the source parameters are within this mass and redshift bin – is exactly what is meant by the error kernel in Eq. 15. The marginalised

error kernel is thus

$$K(\hat{\lambda}_i|\lambda_i) = \frac{1}{N} \sum_{\mu=1}^{N} \frac{1}{\sqrt{2\pi\sigma_{i,\mu}^2}} \exp\left[-\frac{\left[\hat{\lambda}_i - \lambda_i\right]^2}{2\sigma_{i,\mu}^2}\right], \qquad (16)$$

where $\sigma_{i,\mu}$ is the uncertainty in the ith parameter in the μth randomly generated set of source parameters within the bin. N is the total number of samples generated in the bin.

Although each individual element of the sum is a Gaussian, the process results in a non-Gaussian distribution since the size of the uncertainty, $\sigma_{i,\mu}$, changes with each new set of sample parameters. This can be seen by comparing Figures 1a and 1b. The sum of Gaussians, all centred on the value of the source parameter, has a taller peak and fatter tails than a single Gaussian with average standard deviation $\left[\sum_{\mu=1}^{N} \sigma_{i,\mu}^2\right]^{0.5}/N$.

There are two limitations in the way we have generated the error kernel that stem from our use of the linear least-squares LISA Calculator. First, sources at moderate redshift and large sigma will have tails that extend to low z, even though a true nearby source would not be confused with a stronger source at moderate redshift. Production of the true PDF for such a case would involve a more complete algorithm, avoiding the limitations of linear least-squares analysis and resulting in a shorter low-z tail. Second, the LISA Calculator, like many least-squares tools, drops an ill-determined parameter when the information matrix is singular, and gives an inappropriately low sigma for the remaining parameters. This did occur in a number of the cases we ran and contributed some anomalously strong peaks to the Monte Carlo averaging.

Our covariance studies found that the fractional uncertainties in the redshifted mass variables were always much less than the fractional uncertainties in redshift (see figure 2), and are insignificant compared to our coarse mass binning[4]. For the purposes of this initial study, we have ignored the mass errors and considered only the distribution of the detected redshifts. The error kernel is thus

$$K_i(\hat{z}, z) = \frac{1}{N_i} \sum_{\mu_i} \frac{1}{\sqrt{2\pi\sigma_{z,\mu_i}^2}} \exp\left[-\frac{(\hat{z} - z)^2}{2\sigma_{z,\mu_i}^2}\right], \qquad (17)$$

where i corresponds to one of the mass ranges defined in Table 1 and where the sigmas are understood to be the uncertainties determined for each mass bin. Thus, our Monte Carlo study returns three error kernels at a given redshift, one for each mass range. Each error kernel consists of a set of PDFs, one PDF for each redshift bin $\hat{z}$. These source redshifts are uniformly spaced between 0 and 20 (see figure 1c). Each of these PDFs represent Monte Carlo averages of LISA calculator Gaussian PDFs, varied over the *sample* parameters and the mass parameter ranges listed in Table 1. Each error kernel contains about 2 million LISA calculator runs. One may get a feel for the shape of the entire kernel by looking at the 70% confidence intervals shown in Figure 1d.

---

[4]Rest-frame variables with dimensions of mass will have an error that is 100% correlated with the error in the redshift, a detail we will investigate in future work.
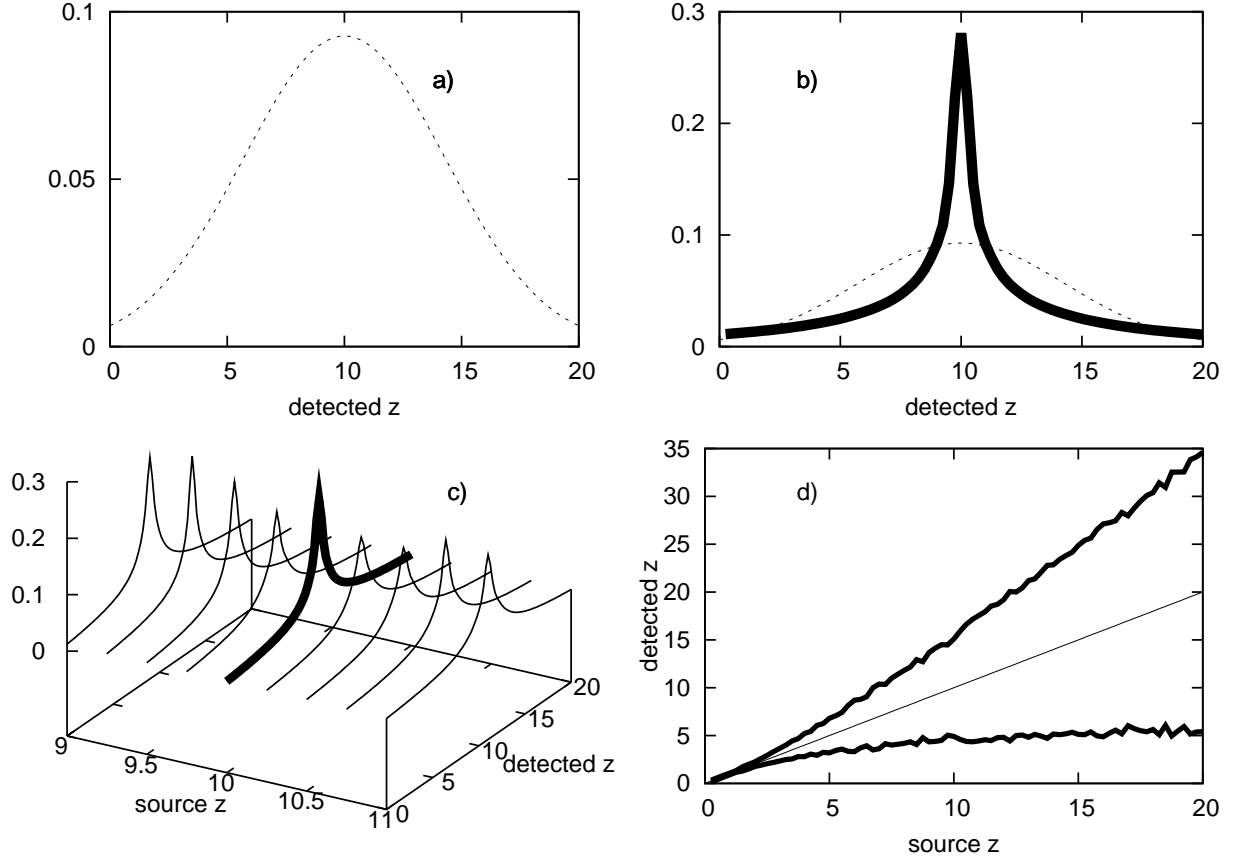
Fig. 1.— Creating the error kernel for the 'medium mass' bin and marginalised parameters described in Table 1, total masses between $10,000 M_\odot$ and $100,000 M_\odot$. a) The Gaussian PDF implied by simple RMS error. b) Adding the probability densities resulting from many different marginalised parameters results in a highly non-normal distribution. Shown here (in solid black) is the distribution of possible detections given several hundred sources at a redshift of 10 in a mass range $10^4 : 10^6 M_\odot$. Overlaid (in dashes) is the distribution obtained by simply adding the errors in quadrature. c) The $z_s = 10$ PDF inserted into its place in the error kernel. Source redshifts are sampled at even redshift intervals of 0.25. d) 70% confidence intervals for LISA determination of redshift gives an overview of the resulting error kernel.
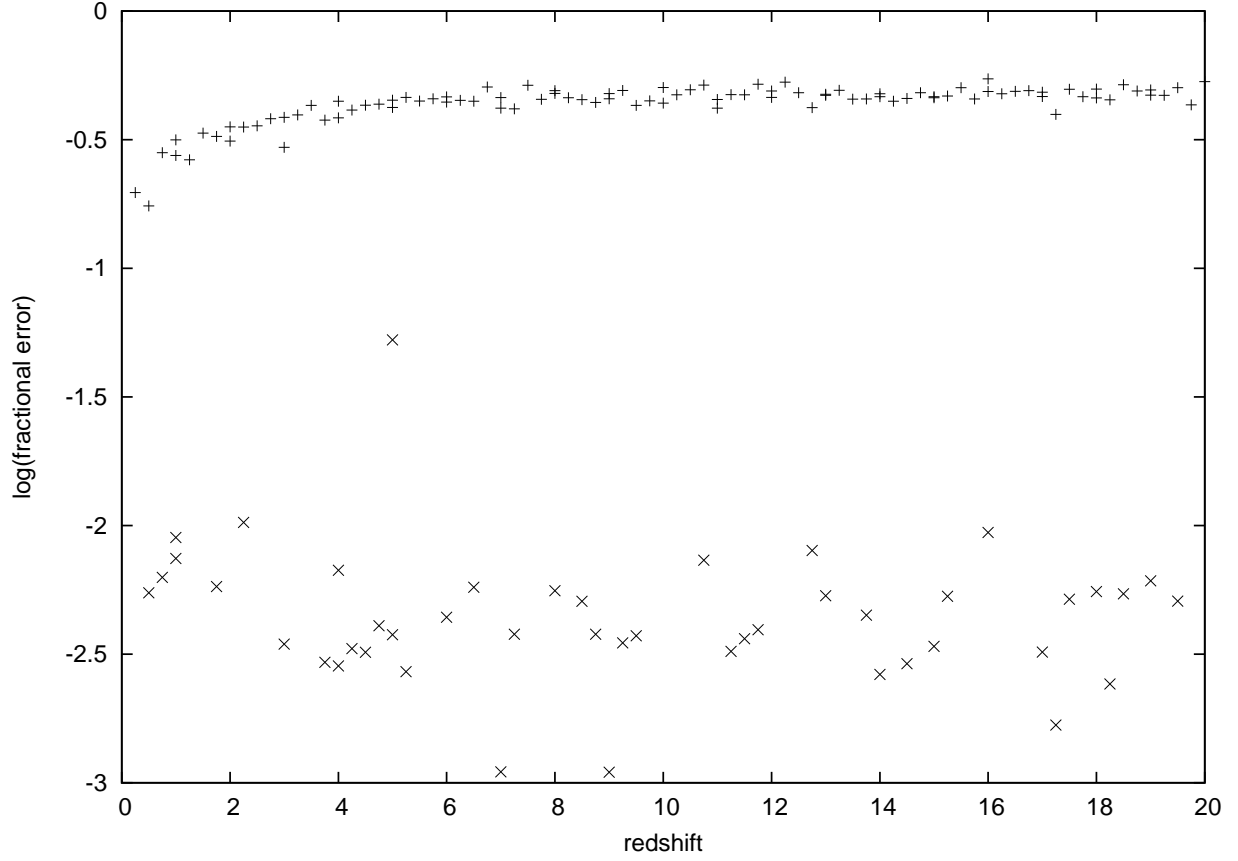
Fig. 2.— Average fractional error for binaries with total mass between $10,000M_\odot$ and $1,000,000M_\odot$ and reduced mass between 0.001 and 0.25, using + for redshift and x for reduced mass. Chirp mass errors are not shown, but are an order of magnitude below the reduced mass errors. Error in redshift dominates the reduced mass error by over an order of magnitude.

4.2. Applying the Error Kernel

Once the error kernel in Eq. 17 has been calculated, it may be applied to any population model that gives the source coalescence rate in the corresponding mass (i) and redshift bin $\Gamma_i(z)$, producing a prediction for the detected coalescence rate, $\Gamma'_i(\hat{z})$. This is accomplished by a straightforward convolution, which we write in continuum form as

$$\Gamma'_i(\hat{z}) = \int_0^{z_{\max}} \Gamma_i(z) \times K_i(\hat{z}, z) dz. \tag{18}$$

As we noted in Eq. 15, some of the binaries sampled will have signal-to-noise ratios too small to be detectable, regardless of the error in the parameters. Previous analysis by Sesana et al. (2007) has used the fiducial SNR limit of 5. We chose to use a cutoff at SNR $= 8$, but the number of additional sources dropped due to our more conservative cutoff was negligible. The PDFs of binaries which do not make the SNR cutoff should not be included in the error kernels, but the proportion of rejected binaries in each source parameter bin must still be taken into account when the error kernels are applied to the models. Therefore, the error kernels (which would otherwise normalise to 1) are weighted with the fraction of binaries in each bin, $\epsilon_i(z)$, having SNR ≥ 8. Taking this detectability into account, the convolved coalescence rates may be written

$$\Gamma'_i(\hat{z}) = \int_0^{z_{\max}} \Gamma_i(z) \times \epsilon_i(z) \times K_i(\hat{z}, z) dz. \tag{19}$$

5. Discriminating Between Population Models

As an illustration of LISA's ability to discriminate between black hole population models, we consider four formation models. The models we have chosen for the demonstration – those by Volonteri et al. (2003), Koushiappas et al. (2004), and two by Begelman et al. (2006), one with 'high' feedback and one with 'low' feedback, (hereafter VHM, KBD, BVRhf, and BVRlf respectively) – are variations on the extended Press-Schecter (EPS) formalism by Lacey & Cole (1993) which assigns a mass-dependent probability to halo mergers. Key variations between these models are their assumptions for accretion, their binary hardening scenarios, their choices for mass and redshift of seed formation, and the details of the way they handle MBH binary interactions near the merger.

5.1. Convolving The Models with the LISA Error Kernel

The effect of the error kernel on population model testing can be seen in Figure 3, where we have taken the VHM model with its three mass bins lumped together, spanning the range from $300\ M_\odot$ to $10^8 M_\odot$. The VHM model, with its unique seeding scenario, predicts a large number of low mass, high redshift binaries. The distribution, shown as the large-amplitude solid curve in Figure 3, peaks and then rolls off sharply at $z \approx 17$. The number of sources in this model that are

expected to be visible with LISA, using a SNR> 8 cut-off relative to the averaged sensitivity curve from the SCG, is given by the low-amplitude dotted curve (see Sesana et al. 2007). The dashed curve represents our results, produced by integrating the model with the kernel, as in Eq. 18. It gives predictions for the distribution of best-fitting parameters detected by LISA, using a cutoff at SNR = 8. The obvious point to be made is that the redshift uncertainties smear out a model's features, so that, while the VHM model of Figure 3 has a very distinctive shape in its theoretical incarnation, the distribution that would be observed by LISA will be far less so.

The presence of detected sources at very low ($z < 2$) redshifts, where the VHM population model says that there should be very few, is a result of the excessively large low-z tails of the error kernel discussed in Section 4. The less sharply peaked shape of the error kernel results as compared with the Sesana results, however, is a consquence of applying detection errors to the redshifts, and will persist even when more robust error-estimation techniques are employed.

Even with our SNR cutoff, we predict more visible sources (179 vs. 96) than did Sesana et al. (2007). This is due in part to our error kernel, with its use of the logarithmic mass distributions within the large mass bins found in the literature, having more massive binaries at high redshift than is actually the case for the VHM models. We also found a puzzling discrepancy in Sesana et al. (2007) between their stated event counts (250 for the VHM model with a 3 year range of coalescence times) and the event counts found by integrating the curves in their figure 1 (over 400 for the same case). Since our model event rates were obtained by extracting the curves from that figure, this discrepancy could also contribute to the differing number of visible sources.

5.2. Discriminating Between Models

For the four models we have chosen to consider as illustrative examples, the results of the error kernel convolutions are shown in Figure 4. The graph in the upper left is for all masses and the other three graphs represent the three mass bins we used. We use a modified version of the Kolmogorov-Smirnov (K-S) test as a measure of separability of the models. Our test differs from the K-S test in that it is sensitive to differences in the model event rates as well as to the cumulative distribution functions (CDFs) of samples drawn from the models. For each pair of models shown in Table 2, we have simulated Monte Carlo draws of the number of sources in each redshift bin, using a Poisson distribution with probability given by each of the models. One thousand draws were taken for each model and our test statistic was calculated, finding the greatest deviation between the cumulative histograms of the two models. The probability that the two draws were from the same model was then found by Monte Carlo sampling from the null hypothesis that the two samples have the same CDF and have event counts which are Poisson distributed with identical rate parameters.

Several comparisons were done between the four models chosen from Sesana et al. (2007). For each comparison, we assumed one year of LISA observations and randomly drew coalescence parameters using the probability distributions for the two models being compared. In each set of
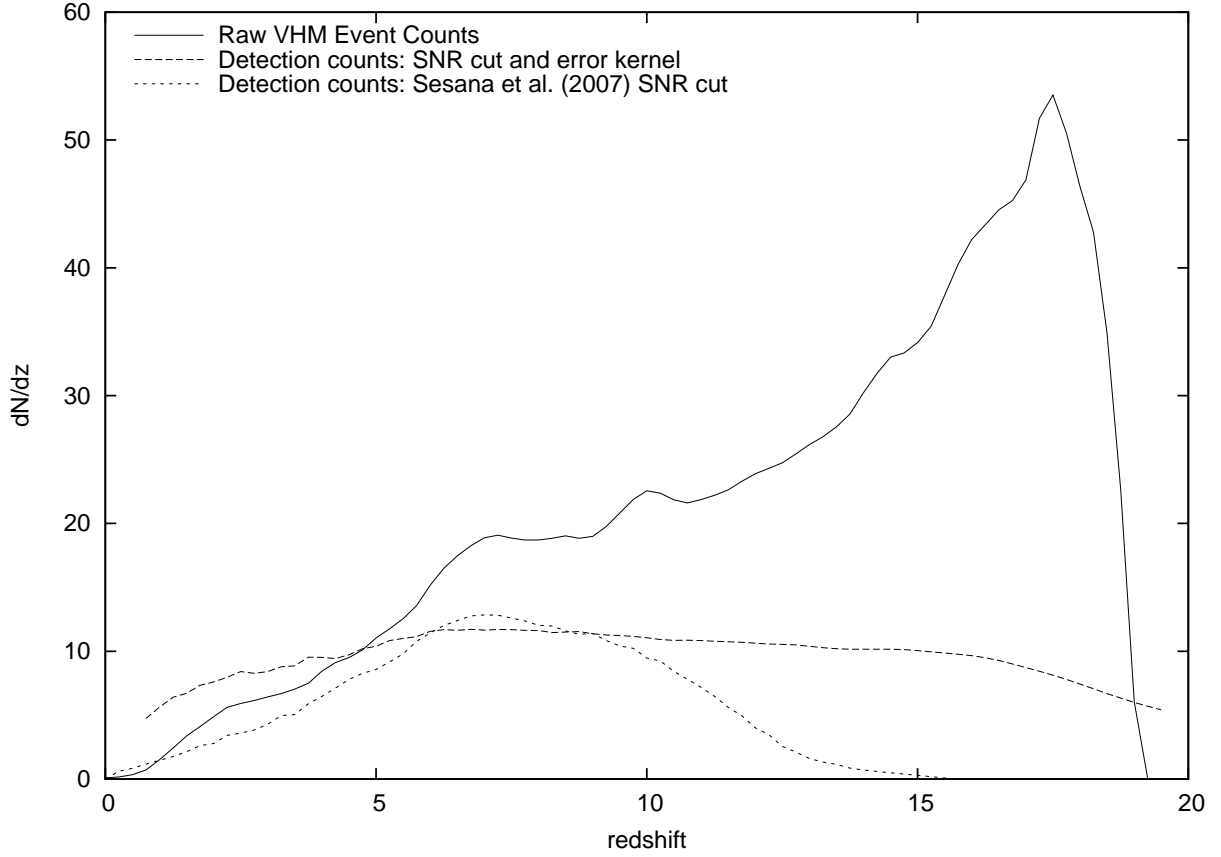
Fig. 3.— The effect of the LISA error kernel on the MBH binary population predicted by Volonteri et al. (2003) for a 3 year observation. Solid line: modelled source distribution for masses below $10^8 M_\odot$. Dotted line: modelled source distribution with SNR > 8 cut, as applied by Sesana et al. (2007). Dashed line: convolution of modelled source distribution with LISA error kernel. The error kernel distribution incorporates the large errors inherent to binary redshift determination.
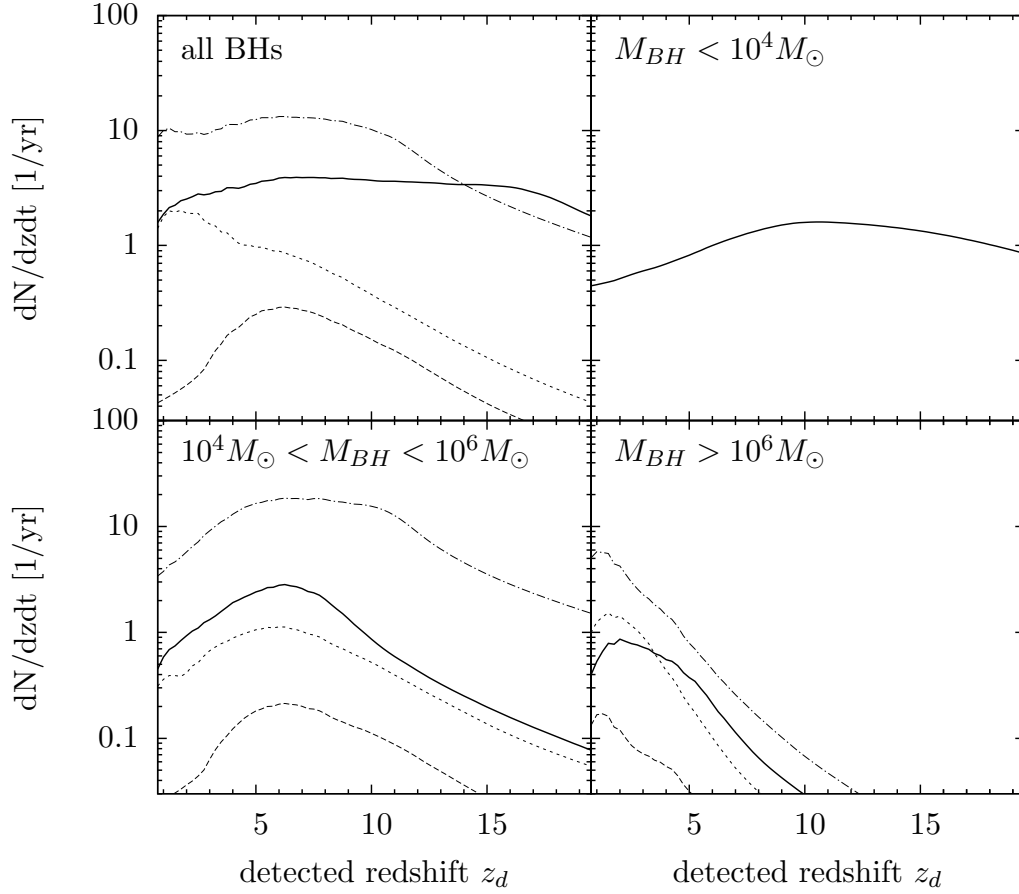
Fig. 4.— Binary merger redshift spectra, after smearing by the LISA error kernel in the style of Sesana et al. (2007). Solid line - VHM, short-long dashed line - KBD, short dashed line - BVRlf, dashed line - BVRhf.

draws, our modified K-S statistic, E, was determined and Q, the probability that two such draws would be produced by the same model, was calculated. The results for each random draw were then averaged over one thousand such realisations, giving the values displayed in Table 2. In the two data columns, we show the results from the raw models themselves, with no parameter uncertainties taken into account, and the results from the models after they have been convolved with the LISA error kernel. As can be seen in the table, the probability that any of the simulated data sets for one model might have been produced by one of the other models is small. The models examined here appear to be easily distinguishable from each other, with the exception of the comparison of the BVRhf model with the BVRlf model with its average Q value of 0.055 (corresponding to a rather shaky 94.5% confidence). Even in that case, when we look at the median of Q rather than its mean, we find it to be 0.012 (98.8% confidence), implying that a BVRlf realization can usually be distinguished from a BVRhf realization.

6. Conclusion

In this paper, we have constructed an 'error kernel' for the LISA detector, using a public-domain error computation module in a Monte-Carlo data pipeline, marginalising over the 'sample' parameters. This result represents a first implementation of a model-level error function for a gravitational wave observatory, a concept which is central to all types of astronomy. The error kernel approach introduced here is designed to replace simple SNR cuts as the interface between population modellers and gravitational wave signal specialists.

The error kernel can be computed as a function of any of the population parameters. We have chosen to use redshift alone, but total mass or mass ratio could easily have been added. Once calculated, contours of the error kernel can be used to visualise the relative impact of the detector noise, analysis technique, and choice of parameter binning on the ability of the detector to determine the parameters of the sources in the model.

We reiterate that we are limited by working with the models as published, with their emphasis on redshift as the parameter of interest, rather than having access to more detailed model results giving populations as functions of masses and redshifts. In particular, while the logarithmic intra-bin mass distribution is as reasonable a choice as any other, the mass bins published in the literature are so large that no model-independent distribution can produce an error kernel that is free from significant bias compared to what would be obtained using the full model results. Furthermore, with LISA's exquisite resolution in the redshifted mass variables, the mass distribution is likely to provide useful astrophysical information in its own right. It is our opinion that a mass resolution of at least 1 bin per decade over the range $10^2 \ldots 10^6 M_\odot$ is necessary to meaningfully specify the mass dependence of these populations. We are currently working toward improved comparisons using more detailed models.

The demonstration in this paper for four model comparisons looks at the distinguishability of

Binary Parameter	Marginalisation Range(s)	
ψ	$0 : \pi$	
ι	$0 : \pi/2$	
θ	$0 : 2\pi$	
ϕ	$-\pi/2 : \pi/2$	
Φ_0	$0 : \pi$	
t_c	0:4 years	
η	$0.0025 : 0.25$	
z	Not Marginalised	
M_{tot}	$250 : 10^4 M_\odot$	Low Mass Case
	$10^4 : 10^6 M_\odot$	Medium Mass Case
	$10^6 : 10^8 M_\odot$	High Mass Case

Table 1: This table of parameters lists the completely marginalised case parameters (grey boxes) along with their ranges and describes the treatment of the three population parameters. Reduced mass ratio η is averaged, z is held constant and total mass (M_{tot}) is divided into three units.

Models Compared	Before LISA kernel		After LISA Kernel	
	$\langle E \rangle$	$\langle Q \rangle$	$\langle E \rangle$	$\langle Q \rangle$
VHM - KBD	175.6	$< 10^{-4}$	90.5	$< 10^{-4}$
VHM - BVRlf	119.7	$< 10^{-4}$	49.7	$< 10^{-4}$
VHM - BVRhf	132.9	$< 10^{-4}$	58.9	$< 1.0 \times 10^{-4}$
BVRhf - BVRlf	14.29	0.021	9.82	0.055

Table 2: Comparisons of models before and after convolution with LISA kernel, for binaries coalescing within the observation window, assuming one year of observation time. The 'Before LISA' comparisons effectively assume that all of the sources are detectable and have zero redshift error, while the 'After LISA' comparisons incorporates the effects of both parameter uncertainty and detectability. E is the maximum deviation between the cumulative histograms of random draws from the two models. Q is the corresponding probability that random fluctuations could be responsible for the deviation.

the models based on what might eventually be a catalogue of LISA binaries. Our approach has been to do a forward modelling from the relevant parameters of the population model to the detected parameters of sources seen in the LISA data. The fact that those predictions are statistically different suggests that LISA data will have appreciable model-discriminating power.

When the LISA data are finally available, the analysis will include backward, Bayesian, modelling which calculates and interprets the contribution of each detected source to a likelihood function for the models being tested. This backward population analysis framework will be an essential component of future LISA data analysis, and is a natural direction of our future work in the long term.

REFERENCES

Becker R. H., Fan X., White R. L., Strauss M. A., Narayanan V. K., Lupton R. H., Gunn J. E., Annis J., Bahcall N. A., Brinkmann J., Connolly A. J., Csabai I., Czarapata P. C., Doi M., Heckman T. M., Hennessy G. S., Ivezić Ž., Knapp G. R., Lamb D. Q., McKay T. A., Munn J. A., Nash T., Nichol R., Pier J. R., Richards G. T., Schneider D. P., Stoughton C., Szalay A. S., Thakar A. R., York D. G., 2001, AJ, 122, 2850

Begelman M. C., Volonteri M., Rees M. J., 2006, MNRAS, 370, 289

Bender R., 2005, Growing Black Holes, Merloni A., Nayakshin S., Sunyaev R. A., eds., Springer

Bromm V., Loeb A., 2002, ApJ, 575, 111

Crowder J., Cornish N., 2006, Lisa calculator. http://www.physics.montana.edu/lisa/lisacalculator/

Crowder J. O., 2006, PhD thesis, Montana State University, United States – Montana

Cutler C., Flanagan É. E., 1994, Phys. Rev. D, 49, 2658

Djorgovski S. G., Volonteri M., Springel V., Bromm V., Meylan G., 2008, ArXiv e-prints

Ebisuzaki T., Makino J., Tsuru T. G., Funato Y., Portegies Zwart S., Hut P., McMillan S., Matsushita S., Matsumoto H., Kawabe R., 2001, ApJ, 562, L19

Fan X., Narayanan V. K., Lupton R. H., Strauss M. A., Knapp G. R., Becker R. H., White R. L., Pentericci L., Leggett S. K., Haiman Z., Gunn J. E., Ivezić Ž., Schneider D. P., Anderson S. F., Brinkmann J., Bahcall N. A., Connolly A. J., Csabai I., Doi M., Fukugita M., Geballe

T., Grebel E. K., Harbeck D., Hennessy G., Lamb D. Q., Miknaitis G., Munn J. A., Nichol R., Okamura S., Pier J. x., Prada F., Richards G. T., Szalay A., York D. G., 2001, AJ, 122, 2833

Ferrarese L., Merritt D., 2000, ApJ, 539, L9

Flanagan É. É., Hughes S. A., 1998a, Phys. Rev. D, 57, 4535

—, 1998b, Phys. Rev. D, 57, 4566

Gebhardt K., Bender R., Bower G., Dressler A., Faber S. M., Filippenko A. V., Green R., Grillmair C., Ho L. C., Kormendy J., Lauer T. R., Magorrian J., Pinkney J., Richstone D., Tremaine S., 2000, ApJ, 539, L13

Haehnelt M. G., Kauffmann G., 2000, MNRAS, 318, L35

Hellings R. W., Moore T. A., 2003, Classical and Quantum Gravity, 20, 181

Jennrich O., 2004, in Society of Photo-Optical Instrumentation Engineers (SPIE) Conference Series, Vol. 5500, Society of Photo-Optical Instrumentation Engineers (SPIE) Conference Series, Hough J., Sanders G. H., eds., pp. 113–119

Kormendy J., Richstone D., 1995, ARA&A, 33, 581

Koushiappas S. M., Bullock J. S., Dekel A., 2004, MNRAS, 354, 292

Lacey C., Cole S., 1993, MNRAS, 262, 627

Lang R. N., Hughes S. A., 2006, Phys. Rev. D, 74, 122001

Larson S. L., 2000, Online sensitivity curve generator. `http://www.srl.caltech.edu/~shane/sensitivity/`, based on S. L. Larson, W. A. Hiscock & R. W. Hellings, 2000, Phys. Rev. D **62**, 062001

Madau P., Rees M. J., 2001, ApJ, 551, L27

Magorrian J., Tremaine S., Richstone D., Bender R., Bower G., Dressler A., Faber S. M., Gebhardt K., Green R., Grillmair C., Kormendy J., Lauer T., 1998, AJ, 115, 2285

Merritt D., Ferrarese L., 2001, ApJ, 547, 140

Moore T. A., Hellings R. W., 2002, Phys. Rev. D, 65, 062001

Ohkubo T., Nomoto K., Umeda H., Yoshida N., Tsuruta S., 2009, ArXiv e-prints

Ohkubo T., Umeda H., Maeda K., Nomoto K., Suzuki T., Tsuruta S., J Rees M., 2008, in American Institute of Physics Conference Series, Vol. 990, First Stars III, O'Shea B. W., Heger A., eds., pp. 244–246

Ohkubo T., Umeda H., Maeda K., Nomoto K., Suzuki T., Tsuruta S., Rees M. J., 2006, ApJ, 645, 1352

Portegies Zwart S. F., Baumgardt H., Hut P., Makino J., McMillan S. L. W., 2004a, Nature, 428, 724

Portegies Zwart S. F., Dewi J., Maccarone T., 2004b, MNRAS, 355, 413

Rees M. J., 2002, Lighthouses of the Universe, M. Gilfanov M., Sunyaev R. A., Churazov E., eds., Berlin: Springer

—, 2003, The Future of Theoretical Physics and Cosmology, Gibbons G., Shellard E., Rankin S., eds., Cambridge University Press

Richstone D., Ajhar E., Bender R., Bower G., Dressler A., Faber S., Filippenko A., Gebhardt K., Green R., Ho L., et al., 1998, Nature, 395, A14

Sesana A., Haardt F., Madau P., Volonteri M., 2004, ApJ, 611, 623

Sesana A., Volonteri M., Haardt F., 2007, MNRAS, 377, 1711

Somerville R. S., Kolatt T. S., 1999, MNRAS, 305, 1

Stern D., Spinrad H., Eisenhardt P., Bunker A. J., Dawson S., Stanford S. A., Elston R., 2000, ApJ, 533, L75

Tanaka T., Haiman Z., 2009, ApJ, 696, 1798

Thorne K. S., 1987, 300 Years of Gravitation, Israel W., Hawking S. W., eds., Cambridge University Press, pp. 330–458

Tremaine S., Gebhardt K., Bender R., Bower G., Dressler A., Faber S. M., Filippenko A. V., Green R., Grillmair C., Ho L. C., Kormendy J., Lauer T. R., Magorrian J., Pinkney J., Richstone D., 2002, ApJ, 574, 740

Tsuruta S., Ohkubo T., Umeda H., Maeda K., Nomoto K., Suzuki T., Rees M. J., 2007, in IAU Symposium, Vol. 238, IAU Symposium, Karas V., Matt G., eds., pp. 241–246

Umeda H., Yoshida N., Nomoto K., Tsuruta S., Sasaki M., Ohkubo T., 2009, Journal of Cosmology and Astro-Particle Physics, 8, 24

Vallisneri M., 2008, Phys. Rev. D, 77, 042001

Vallisneri M., Mock LISA Data Challenge Taskforce, 2006, in Bulletin of the American Astronomical Society, Vol. 38, Bulletin of the American Astronomical Society, pp. 992–+

Volonteri M., Madau P., Haardt F., 2003, ApJ, 593, 661

Zheng W., Tsvetanov Z. I., Schneider D. P., Fan X., Becker R. H., Davis M., White R. L., Strauss M. A., Anderson Jr. J. E., Annis J., Bahcall N. A., Connolly A. J., Csabai I., Davidsen A. F., Fukugita M., Gunn J. E., Heckman T. M., Hennessy G. S., Ivezić Ž., Knapp G. R., Lupton R. H., Peng E., Szalay A. S., Thakar A. R., Yanny B., York D. G., 2000, AJ, 120, 1607